Simulation of optical remote sensing scenes with application to the EnMAP hyperspectral mission

L. Guanter, K. Segl, H. Kaufmann

Abstract— The simulation of remote sensing images is a useful tool for a variety of tasks, such as the definition of future Earth Observation systems, the optimization of instrument specifications, and the development and validation of data processing algorithms. A scene simulator for optical hyperspectral and multispectral data has been implemented in the frame of the Environmental Mapping and Analysis Program (EnMAP) mission. EnMAP is a German built hyperspectral space sensor scheduled for launch in 2012. EnMAP will measure in the 420-2450 nm spectral range at a varying spectral sampling of 6.5-10 nm. Images will cover 30 km×30 km areas at an approximate ground sampling distance of 30 m. The EnMAP scene simulator presented in this paper is able to generate realistic EnMAP-like data in an automatic way under a set of user-driven instrumental and scene parameters. Radiance and digital numbers data are generated by 5 sequential processing modules which are able to produce data over a range of natural environments, acquisition and illumination geometries, cloud covers and instrument configurations. The latter include the simulation of data non-uniformity in the spatial and spectral domains, spatially coherent and non-coherent instrumental noise and instrument's modulation transfer function. Realistic surface patterns for the simulated data are provided by existing remote sensing data in different environments, from dry geological sites to green vegetation areas. A flexible radiative transfer simulation scheme enables the generation of different illumination, observation and atmospheric conditions. The methodology applied to the complete scene simulation and some sample results are presented and analyzed in this paper.

Index Terms— Scene simulation, EnMAP, imaging spectroscopy, non-uniformity, radiative transfer, instrumental noise

I. INTRODUCTION

The recognized potential of imaging spectroscopy [1]–[3] to provide more and better information about the Earth system than multispectral instruments is currently not counterbalanced by an equivalent availability of hyperspectral satellite data. There is already a long record of airborne-based imaging spectroscopy, which includes traditional programs like the Airborne Visible/Infrared Imaging Spectrometer (AVIRIS) [4], [5] or HyMAP [6], and a new generation of upcoming instruments, like the Airborne Reflective Emissive Spectrometer (ARES) [7] and the Airborne Prism Experiment (APEX) [8]. However, only former technology demonstrators like Hyperion on EO-1 [9] and the Compact High Resolution Imaging Spectrometer on board the Project for On Board Autonomy (PROBA/CHRIS) [10] can provide space-scale time-resolved hyperspectral data. Even though EO-1 Hyperion and

L. Guanter, K. Segl and H. Kaufmann are with the Helmholtz Centre Potsdam, German Research Centre For Geosciences GFZ, Remote Sensing Section, Telegrafenberg, D-14473, Potsdam, Germany (email: luisguan@gfz-potsdam.de).

TABLE I

SUMMARY OF ENMAP SENSOR AND ORBIT PARAMETERS ACCORDING TO THE MISSION REQUIREMENT DOCUMENT.

Imaging principle	Pushbroom-prism
Spectral range	VNIR: 420-1000 nm
	SWIR: 900-2450 nm
Mean SSI	VNIR: 6.5 nm
	SWIR: 10 nm
SNR at reference radiance	>500:1@ 495 nm (VNIR)
	>150:1@2200 nm (SWIR)
Spectral calibration accuracy	VNIR: 0.5 nm
	SWIR: 1 nm
Spectral stability	0.5 nm
Radiometric calibration accuracy	<5%
Radiometric stability	<2.5%
Radiometric resolution	14 bit
Sensitivity to polarization	<5%
Spectral smile/keystone effect	<20% of detector element
GSD	30 m
Swath width	30 km
Geometric co-registration	0.2×GSD
Swath length (at least)	1000 km/orbit
Coverage	Global in
	near-nadir mode (VZA≤5°)
Target revisit time	23 days (VZA≤5°)
	4 days (VZA≤30°)
Pointing accuracy	100 m at sea level

PROBA/CHRIS systems are currently providing key data as precursors of spaceborne imaging spectroscopy, the spatial coverage they offer may not be enough for some applications, and issues such as data uniformity, reliable radiometric and spectral calibration and data pre-processing are yet to be solved.

The Environmental Mapping and Analysis Program (EnMAP) [11] German hyperspectral mission is intended to fill this gap. A summary of some mission parameters as they appear in the mission requirement document (MRD) is displayed in Table I. EnMAP is designed to sample areas of 30 km×30 km with a ground sampling distance (GSD) of 30 m, measuring in the 420-2450 nm range by means of two entirely independent prism-based spectrometers covering the visible to near-infrared (VNIR) and the short-wave infrared (SWIR) spectral regions. The mean spectral sampling interval (SSI) and resolution is of 6.5 nm in the VNIR, and of 10 nm in the SWIR. Accurate radiometric and spectral responses are guaranteed by a required signal-to-noise ratio (SNR) about 500:1 in the VNIR and 150:1 in the SWIR for a given mission reference radiance level, radiometric calibration accuracy better than 5% and spectral calibration uncertainty of 0.5 nm in the VNIR and of 1 nm in the SWIR. An across-track pointing capability of up to 30° enables a target revisit time of 4 days.

The orbit has a repeat cycle of 23 days, providing global coverage for view zenith angles (VZAs) smaller than 5°. The EnMAP mission entered into the construction phase (phase-C) in November 2008, while the launch is currently scheduled for 2012.

From the scientific perspective, current EnMAP preparatory activities are focused on the support of mission requirements consolidation and instrument concept development. Extensive sensitivity analyses are to be performed in order to estimate the impact of different instrumental or environmental parameters on the signal measured by the sensor. A careful simulation of reflectance, top-of-atmosphere (TOA) radiance and digital numbers (DNs) under different instrumental and environmental configurations is fully necessary for the optimization of system requirements and the derivation of expected error budgets [7], [12]–[16]. For the study of instrumental radiometric and spectral response, analyses can be based on 1D radiance or DN spectra. However, the spatial dimension must also be taken into account when those parameters describing the instrument spatial performance, like the modulation transfer function (MTF), the keystone effect or spectrometer co-registration, are to be evaluated [17]. Moreover, synthetic images recreating realistic environmental conditions and generated with the proper format are also very useful as a test-bench for future algorithm development, both for the pre-processing chain and the scientific exploitation of the data.

For those reasons, we have designed and implemented a scene simulator for optical remote sensing data, with special emphasis on EnMAP data simulation. No commercial package suitable of being adapted to this purpose was found, so all the modules were newly developed. However, approaches to hyperspectral data simulation already in the literature were reviewed and considered in order to avoid repetition (e.g. [18]–[25]). The present approach intends to address the entire simulation process carefully, from spatially- and spectrally-oversampled reflectance and atmospheric data to the final DN data convolved to the instrument's spatial and spectral responses. Special attention has been put on the challenging task of the accurate simulation of non-uniformities in the spatial domain, such as keystone and spectrometer co-registration, as it was requested by the EnMAP double-slit concept during the instrument design phase. Moreover, in order to make the simulated images to be a useful reference data set for pre-processing and scientific algorithms development, a considerable effort has been put on the recreation of a range of environmental conditions. Different natural environments, including vegetation, bare soil, mineral-rich areas and water bodies, have been generated following realistic spatial distribution patterns. Cloud covers, cloud shadows and multitemporal acquisitions are also generated following physically-based approaches. From our understanding, this capability to reproduce realistic cloud patterns and temporal changes using physical approaches represent a step further with respect to the state of art in the simulation of optical remote sensing scenes.

A detailed description of the scene simulator is provided in this paper. The modules compounding the simulator are reviewed in Section II. Exemplary results from these modules and other quality-analyses performed on the data are presented in Section III. The main points are finally summarized in Section IV. It must be noted that most of the data about the EnMAP instrument configuration appearing in this work are either simulated or from an earlier instrument concept. A detailed description of the last EnMAP design can be found in [26].

II. METHODOLOGY DESCRIPTION

A. General aspects

Even though the simulator is implemented in a modular and flexible way so that it can be applied to different optical sensor configurations, some of the parameters and processing steps are optimized for the EnMAP configuration. For this reason, it will be referred to as "EnMAP simulator" hereinafter. In the EnMAP version, the simulator covers the 400-2500 nm spectral region and generates radiance and DN images of 1000×1000 pixels with a GSD of 30 m. In the most general simulation configuration, input data are at SSI of 1 nm and GSD of about 3 m. This enables the later convolution to the final 6.5-10 nm SSI and 30 m GSD of EnMAP. Those input data could be changed if the simulator had to be applied to systems with different spectral or spatial specifications.

The most important bottleneck for the automatic generation of simulated images is the lack of high spatial resolution data covering an area of 30 km×30 km. Spectral libraries and image classification techniques are used together with those high spatial resolution data for the recreation of realistic spatial and spectral patterns in the images. Data acquired by Système Pour l'Observation de la Terre (SPOT) [27] can be used for some purposes, but the resolution and the spectral sampling are too poor for some other. An alternative is to use airborne hyperspectral data, which can provide enough resolution to cover the 30 km at the desired ∼3 m resolution along the acquisition across-track direction, which is normally the spatial dimension in pushbroom instruments [28]. Even though these approaches are necessary for the evaluation of spatial parameters, data availability is a serious obstacle for the simulation of large data sets including a variety of target types. For this reason, the simulator can work under two different modes, with and without spatial analysis. When no spatial analysis is to be performed, input reflectance data are directly generated at nearly-30 m using other data sources (e.g. Landsat [29], PROBA/CHRIS and Hyperion archives).

As depicted in Fig. 1, the simulator consists of 5 independent modules:

1) *Reflectance Module*, which generates the original noise-free reflectance map that is converted to radiance and DN by the subsequent modules, at either ∼3 m or 30 m GSD and 1 nm SSI.
2) *Spatial Module*, which performs the spatial resampling to the final 30 m GSD when required, taking into account the real instrument MTF and spatial non-uniformity sources (spectrometer co-registration, keystone and telescope smile and distortion).
3) *Atmospheric Module*, which converts from surface reflectance to TOA radiance data considering pixel-wise horizontal distributions of aerosol optical thickness
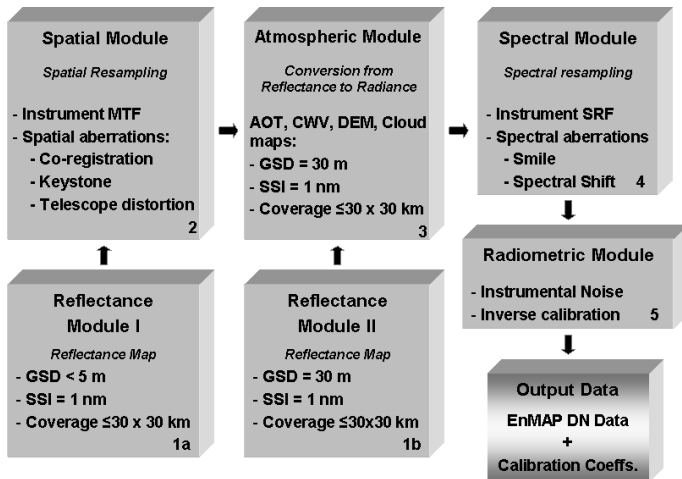
Fig. 1. Schematic view of the simulation flow in the EnMAP simulator.

(AOT) and columnar water vapor (CWV), surface elevation (DEM), and cloud covers and shadows.

4) *Spectral Module*, which performs the convolution of the high spectral resolution TOA radiance data to the instrument spectral response, taking into account the actual spectral response functions (SRFs), and simulating data non-uniformity in the spectral domain, namely spectral curvature effect (smile) and spectrometer shift in the spectral direction.

5) *Radiometric Module*, which simulates spatially coherent and non-coherent noise, dead and bad pixels and calibration coefficients according to the instrument dynamic range.

It can be noted that the spatial module is applied before the atmospheric module in the module sequence depicted in Fig. 1. This violates the real sequence, in which the solar radiation reflected by the surface interacts with the atmosphere before arriving at the sensor. To reproduce this sequence, one should start with the simulation of spatially-oversampled reflectance and atmospheric parameters, that are combined to generate spatially-oversampled TOA radiance, which is the product finally resampled to the 30 m pixel resolution. However, it was demonstrated that there were no appreciable differences at the TOA radiance level between this approach and the one proposed, consisting in degrading spatially-oversampled reflectance maps to 30 m resolution, which are then combined to 30 m resolution atmospheric parameters to generate the 30 m TOA radiance. Substantial advantages are associated to the latter approach in terms of computation burden, as the derivation of pixel-wise atmospheric parameters at $\sim$3 m spatial resolution and with 1 nm of spectral sampling would lead to large data volumes and the corresponding increase of computation time. The error associated to only resampling reflectance data tends to zero in flat terrain, as terrain roughness is the main factor for the horizontal variation of atmospheric parameters.

B. Reflectance module

The reflectance module of the EnMAP scene simulator provides noise-free high spectral resolution reflectance data with realistic horizontal distributions of surface components. This includes vegetation, bare soil patterns, minerals in geological areas and water bodies. The followed approach is based on the combination of spatial patterns in real atmospherically-corrected remote sensing images with high resolution spectral libraries. Comparable approaches were presented in e.g. [19], [23], [30].

The spatial patterns and texture from the input remote sensing images are retrieved by spectral unmixing. A non-negative least squares (NNLS) unmixing algorithm [31] together with a spectral library is used to unmix the input surface reflectance spectra. The spectral library is resampled to the spectral setting of the input data and to the desired output spectral range and sampling, which is of 400-2500 nm and 1 nm SSI for the simulation of EnMAP data. The NNLS performs linear unmixing constrained to positive abundance values using the spectral library resampled to the input data spectral setting. The resulting abundances are used in combination with the spectral library resampled to the output resolution in order to convert from the original remote sensing data, which usually do not cover the necessary spectral range and that normally show residual reflectance errors from atmospheric correction and instrument calibration, to error-free reflectance patterns resolving the 400-2500 nm spectral range at a 1 nm spectral resolution. The spectral library is chosen according to the type of site to be simulated. The maximum number of endmembers to be used in the unmixing depends on the number of spectral channels of the input data. In addition, different endmember combinations can be defined for different regions in the image enabling a user-defined distribution of single endmembers.

The temporal dimension is also considered in the simulated data sets. For this purpose, input reflectance images from the same rural site and different dates generated following a physically-based approach, as opposite to the endmember inversion approach described before, were available. The procedure for the derivation of each of the dates compounding the mutitemporal series is described in [24]. Landsat data from several dates are the input for the derivation of the reflectance maps. The coupled soil-leaf-canopy (SLC) model is first used to invert geophysical parameters such as soil moisture, leaf area index, fraction of brown leaves, chlorophyll content and dry matter. Then, those parameters are input to SLC to for the forward simulation of the top-of-canopy reflectance. Those biophysical parameters may not exactly match the real ones due to Landsat poor spectral sampling, but they are assumed to be valid for the forward simulation because they present realistic values and spatial distributions. The resulting top-of-canopy reflectance maps are ingested by the next module in the simulator. The biophysical parameters are being delivered to the scientific users together with the simulated images for data traceability and algorithm validation.

It is acknowledged that 3D objects are not considered in the simulation process. Finite 3D objects and shadows are considered of second-order importance at the 30 m resolution

of EnMAP, but they could become important at finer resolution data to which the simulator was to be applied. In order to include 3D effects, a completely different simulation approach, dealing with 3D radiative transfer codes, should then be followed. Those codes present high computation times and are normally not suitable for fine spectral resolution simulations as the ones necessary here. The neglection of 3D effects is then considered one of the limitations of the simulator.

C. Spatial module

The spatial module records the pixel information simulating a flight over a 3D-artificial radiance/reflectance image scene. Due to the EnMAP instrument design, consisting in two independent spectrometers, each with its own slit and a prism-based imaging approach, the simulation of data non-uniformities in the spatial domain [17], [28] is one of the challenges of the EnMAP simulator. A detailed simulation set-up comprising the conversion from the 3D geometry of the image scene to the 2D space of the detector and the simulation of spatial aberrations has been implemented. General aspects of the processing are presented in this paper, whereas more detailed information will be subject of a separate paper.

Most of the spatial modules of sensor simulation tools are based on two models, the geometry model and the optical sensor model. The first model describes the geometric relation between the sensor detector elements and the 3D-image scene employing the position and attitude (roll, pitch, yaw) of the sensor and a DEM. The pointing direction of EnMAP is variable and can be changed up to 30 degrees from nadir view. The optical sensor model performs the spatial recording of pixels. This process is characterized by the convolution of the spectral surface information with filter functions along and across flight track representing the sensor specific point spread functions (PSF). The characteristics of the wavelength depending PSFs are defined by the MTF in the Fourier domain incorporating the optical, detector, vibration and motion MTF of the satellite.

In the case of ENMAP, however, the effects of three additional spatial aberrations have to be included in the processing schema:

1) *Keystone*. It is a lateral chromatic aberration intrinsic to pushbroom imaging spectrometers like EnMAP. It is characterized by a shift of each pixel along the spatial direction of the detector array with wavelength. Fig. 2 depicts an arbitrary example of keystone effect based on real data for five selected across-track pixels in a virtual EnMAP VNIR detector array.
   The magnitude of the keystone effect can be optimized within the instrument design. However, it has to be considered that there is physical link between the instrument response in the spatial and the spectral domain. This means that sensitivity analysis of keystone and smile effect must be carried out during the instrument design phase to contrive a well balanced sensor design.
2) *Co-registration*. EnMAP includes two completely independent spectrometers. This is achieved by the separation of the field-of-view at the spectrometer entrance
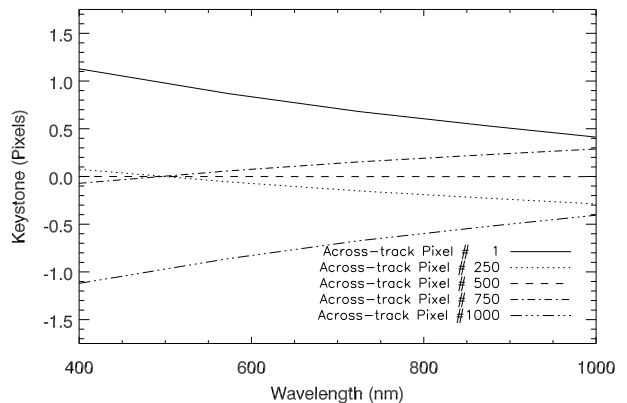

Fig. 2.   Simulated keystone in the VNIR detector based on an earlier EnMAP design.

by means of a double slit, recording corresponding pixels with a time delay of 86.7 ms between VNIR and SWIR detector line. Due to technological limits for manufacturing, pointing stability and Earth rotation a time-dependent error up to 1-2 pixels is possible for the co-registration of the two detectors. It represents the most critical error for a subsequent geometric correction.

3) *Telescope distortion and smile*. This geometrical distortions result from the telescope projection describing the shift of the across track position (distortion) and along track position (smile) from its ideal position. It ranges from 0-1 pixel.

The accurate simulation of all these effects demands a separate calculation for each image pixel and wavelength. It starts with the determination of the true pointing of the selected pixel including the position and attitude of the sensor and all spatial aberrations. The corresponding surface point is calculated applying the associated collinearity equations. The resulting vector defined by the ground point and the pixel represents the center line of a new geometry model differing by a new pitch and roll angle. An adequate spatial subset around the center coordinates is projected to an image grid with unchanged pixel size using the improved collinearity equations. Finally, this projected subset is filtered by the PSF building the intermediate spectral pixel information. Other optional results of the spatial module that spatially fit with the new EnMAP image are two DEMs (one for each detector, as generated for the two different spectrometer acquisition geometries), a geometry image storing the ground coordinates for each pixel and wavelength and adapted feature maps for future parameter retrieval purpose.

D. Atmospheric module

The atmospheric module couples surface reflectance with atmospheric effects in order to generate TOA radiance. If a Lambertian reflectance [32] is assumed, the TOA radiance is given as a function of the surface reflectance and the

atmospheric conditions by

$$L_{\text{TOA}} = L_0 + \frac{1}{\pi} \frac{\rho_s(E_{\text{dir}}\mu_{\text{il}} + E_{\text{dif}})T_\uparrow}{1 - S\rho_s} \qquad (1)$$

where L_{TOA} is the TOA radiance measured by the sensor; L_0 is the atmospheric path radiance; μ_{il} is the cosine of the illumination zenith angle, measured between the solar ray and the surface normal; $E_{\text{dir}}\mu_{\text{il}}$ and E_{dif} are the direct and diffuse fluxes arriving at the surface, respectively; S is the atmospheric spherical albedo, reflectance of the atmosphere for isotropic light entering it from the surface; $T_\uparrow$ is the total atmospheric transmittance (for diffuse plus direct radiation) in the observation direction, and ρ_s is the surface reflectance.

We considered that the inclusion of directional effects in surface reflectance was not necessary according to the use intended for the simulated data. Both in the case of instrument optimization and development of algorithms for single-view data, the Lambertian assumption was considered to be sufficient for the simulation of TOA radiance. No application based on the exploitation of directional information from multiple acquisitions is foreseen for EnMAP at this point. There are two other reasons to justify the Lambertian assumption: on one hand, the realistic simulation of directional effects requires sophisticated models and a large data set of ground measurements, which is not available for the automatic image generation [23], [24]; on the other hand, adding directional effects to the radiative transfer scheme would substantially increase the total computation burden, as the coupling between surface directional effects and atmospheric radiative transfer involves the calculation of time-consuming angular integrals of the bidirectional reflectance distribution function (BRDF) for the entire imaged area [33].

The MODTRAN4 radiative transfer code [34], [35] is used for the calculation of the atmospheric parameters in Eq. 1. MODTRAN4 represents the state-of-the-art radiative transfer code in hyperspectral applications because of the rigorous computation of scattering and absorption processes and the high spectral resolution up to 1 cm^{-1}. However, MODTRAN4 does not directly provide the parameters in Eq. 1, but they must be calculated from the standard output. The path radiance and the diffuse flux arriving at the target are coupled to surface reflectance through multiple scattering in the MODTRAN4 output. In the approach followed in this work, atmosphere and surface contributions are decoupled by means of some algebra performed over MODTRAN4 outputs for two different values of the surface reflectance. This approach is implemented as the so-called ATLUT code, which is fully described in [36].

Apart from VZA, sun zenith angle (SZA) and sun-to-sensor relative azimuth angle (RAA), which are assumed to be constant within the whole image, MODTRAN4 is constrained by variable values of AOT and CWV, as well as surface elevation through a DEM. Pixel-wise distributions of these parameters are generated automatically by interpolation, given a pair of maximum and minimum values defining the variation range and a mathematical function describing horizontal variations.

The standard approach is to generate a large look-up table (LUT) off-line, which covers all the expected input combinations. This LUT provides either the atmospheric parameters or

L_{TOA} by means of n-D linear interpolation in the parameter space [22]. However, this procedure can lead to noticeable errors for those variables not holding a linear relationship with the input parameters, as it is the case of VZA, SZA and RAA [36]. In order to minimize the errors associated to interpolation in the EnMAP simulator, the LUT is generated on-line during each simulation by means of external calls to ATLUT. This LUT consists of 2^3 combinations, the breakpoints being given for the maximum and minimum values of AOT, CWV and DEM. MODTRAN4-ATLUT is run with the exact values of input VZA, SZA, RAA. The time-penalty associated to the 8 runs of ATLUT is counterbalanced by the reduction of the parameter space and the improvement in calculation accuracy.

Atmospheric adjacency effects are also considered in this module. Adjacency effects refer to the scattering of photons reflected by the target's surroundings into the sensor line-of-sight, and define the atmospheric point spread function (aPSF), or equivalently, the atmospheric MTF (aMTF) in the frequency domain. As it was mentioned in the discussion about the spatial resampling to 30 m, it is assumed that the atmospheric MTF can be applied on the reflectance level rather than on TOA radiance, so that it is on reflectance where spatial degradation due to atmospheric effects is simulated. Following [37], the reflectance affected by the adjacency effect, ρ_s^a, can be expressed as a linear combination of the reflectance of the observed pixel ρ_s and the reflectance of the environment $<\rho>$,

$$\rho_s^a = e^{-\tau/\mu_v}\rho_s + t_d <\rho> \qquad (2)$$

the two contributions being weighted by the atmospheric upward transmittance for direct and diffuse radiation ($e^{-\tau/\mu_v}$ and t_d, respectively, with τ the atmospheric optical thickness and $\mu_v = \cos(\text{VZA})$). The aPSF used to derive $<\rho>$ is modulated by the atmospheric state. The parametric formulations presented in [38], [39], based on Monte-Carlo calculations, were implemented in the EnMAP simulator:

$$\text{aPSF}(r) = \frac{1}{2\pi r} \frac{t_d^R F_R'(r) + t_d^A F_A'(r)}{t_d}, \qquad (3)$$

where t_d^R and t_d^A are the diffuse Rayleigh and aerosol transmittances, calculated from MODTRAN4 outputs, and $F_R'(r)$ and $F_A'(r)$ are the derivatives of the environment weighting functions for Rayleigh and aerosol contributions, respectively. Following [40], the aPSF for the target pixel is set to aPSF(R'), where R' is the radius of a circle of the same area than the target pixel. The well-established relation given in [38] was chosen to calculate $F_R(r)$ and $F_A(r)$:

$$F_R(r) = 1 - 0.930 \exp(-0.08r) - 0.070 \exp(-1.10r)$$
$$F_A(r) = 1 - 0.448 \exp(-0.27r) - 0.552 \exp(-2.83r) \qquad (4)$$

Those equations were calculated by means of Monte Carlo simulations by assuming standard vertical profiles of gases and aerosols and a continental aerosol model. Those relationships are assumed to be valid for VZAs $\leq 30°$.

The final step in the atmospheric simulation process is to add clouds and cloud shadows to the images. As in the case of the spatial module, the detailed description of the cloud simulation procedure would be a subject of a separate paper.

In short, a LUT containing TOA radiance as a function of atmospheric and cloud optical parameters, surface elevation, observation and illumination angles, and surface albedo is available. This LUT was generated by the Matrix-Operator MOdel (MOMO) [41], which has a long application history in the field of cloud remote sensing. In order to generate realistic cloud patterns, cloud probability maps [42], [43] calculated from real PROBA/CHRIS images are linked to the cloud optical thickness parameter in the LUT. The surface reflectance in the input images from the reflectance module is in turn linked to the surface albedo in the LUT, so TOA radiance from cloudy pixels is calculated by bilinear interpolation. Shadows are generated as the attenuation of the direct irradiance flux E_{dir}. This attenuation is simulated as a multiplicative factor correlated to the cloud probability. Shadow positions are calculated from the observation and illumination angles and the cloud height.

Cloud simulation can be triggered by the user. It is mostly intended for the testing of cloud screening approaches in the data pre-processing and the simulation of sensor saturation. It is recognized that the presented 1D approach may be too simplistic for an accurate reproduction of the complex 3D radiative transfer of cloud fields. A more elaborated approach including 3D effects, e.g. by Monte Carlo simulations, should be implemented if the simulated data were to be used in the validation of cloud optical properties retrieval algorithms.

E. Spectral module

The spectral module performs the spectral resampling from the 1 nm working resolution of the simulator to the EnMAP spectral configuration. This involves the simulation of the instrument SRF, the spectral resolution and SSI, as well as the spectral non-uniformity, given by smile and spectral shift. For sensors covering the entire VNIR-SWIR spectral range, like EnMAP, the spectral module is implemented so that the spectral range is separated into two regions, each one with a different spectral performance, in order to simulate separate spectrometers. An example of a simulated configuration of two spectrometers with different dispersion characteristics is shown in Fig. 3. The mean spectral sampling distance and resolution are about 6.5 nm for the first spectrometer, and 10 nm for the second. There is also a spectral overlap region (900-1000 nm) intended for different purposes, like spectral calibration assessment, the insurance of smooth spectral transition between spectrometers and the estimation of spatial co-registration errors. Gaussian functions are used to simulate EnMAP SRFs. There is no spectral channel binning proposed for EnMAP, as in e.g. CHRIS [10], so every single spectral pixel in the detector array corresponds to a measuring channel. The shape of those channels is close to a Gaussian function with a full-width at half-maximum (FWHM) 1.2 times larger than the spectral sampling distance. This factor was chosen arbitrarily to avoid undersampling effects.

A key parameter to be analyzed and optimized when designing an imaging spectrometer is the spectral curvature or smile effect [28]. It is an optical aberration typical of pushbroom systems, which causes the spectrometer entrance
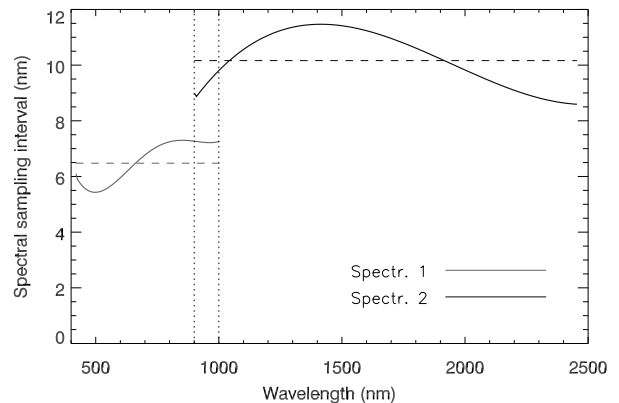

Fig. 3. Simulated spectral sampling interval for the two EnMAP spectrometers. The dashed horizontal lines represent the mean SSI of each spectrometer and the dotted vertical lines the spectral overlap region.
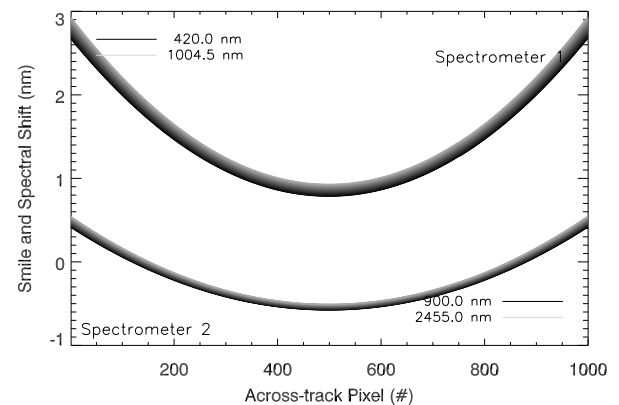

Fig. 4. Simulated smile and spectral shift for the two EnMAP spectrometers based on an earlier EnMAP design.

slit to be projected as a curve on the rectilinear detector array. This originates a combination of bending of spectral lines across the spatial axis, known as smile, which leads to the non-linear variation of spectral channel positions along the spatial direction of the detector array. This results in spectral deviations from a nominal spectral band-setting, usually referenced at the center of the across-track position. Such a deviation increases as the spatial position in the detector array separates from the center. Apart from smile, the mechanical misalignment between the instrument slit and the detector array can also result in a systematic spectral shift which is constant for all the spectral channels and across-track positions in the spectrometer. Smile and a spectral shift of 1 nm in the VNIR and 0.5 nm in the SWIR are simulated in Fig. 4 for the two EnMAP spectrometers. Smile absolute magnitude, smile band-to-band variations, and systematic spectral shifts are spectrometer-dependent parameters in the simulator spectral module. The resampling of the 1 nm TOA radiance to the final EnMAP spectral configuration is performed on a per-column basis in order to include spectral smile.

F. Radiometric module

Once TOA radiance is resampled to the EnMAP spectral configuration, the radiometric module adds noise to the data and performs inverse calibration in order to generate calibration coefficients and the final DN images. Since no detailed model of the instrument electronics is yet available, only multiplicative Gaussian-distributed noise processes are assumed, whose magnitude is given by the SNR requirement in the MRD (about 500:1 in the VNIR, 150:1 in the SWIR). Spatially coherent noise (striping), as well as dead-pixels (those providing a constant read-out) and bad-pixels (those providing a wrong read-out), are simulated according to input values defining the magnitude of striping and the ratio of number of dead/bad pixels to number of normal pixels. Striping and dead- and bad-pixels are randomly distributed within the across-track dimension and the complete 2D space, respectively.

The EnMAP dynamic range is requested to be between a simulated maximum radiance level ($L_{\max}$, given by 90% surface albedo, 0° SZA, target at sea-level and 40 km visibility) and the noise equivalent radiance (NEL), and it is encoded in 14 bits. Spectral gain and offset coefficients describing a linear relationship between radiance and DN are calculated from $L_{\max}$ and NEL. Non-linear instrument response and saturation are simulated out of this range.

III. Example Analyses

The scene simulator has already been applied to the generation of a number of EnMAP-like images under a range of natural environments, atmospheric and instrumental configurations. Color composites from four of those sites are displayed in Fig. 5. The hypercubes are built by stacking the 228 EnMAP bands. A false color composite of the Makhtesh Ramon geological site in Israel (30.57°N, 34.83°E) is displayed in Fig. 5(a). A merge of SPOT-5 multispectral data with the panchromatic (quarter scene), a mineral distribution map and spectral library were used to generate the reflectance data at a 2.5 m GSD following the simulation branch *1a* in Fig. 1. However, a GSD of 3.0 m was assumed to cover an area of 36 km×36 km allowing also the simulation of tilted observation angles. The spatial module of the simulator was then applied in order to resample the data to the EnMAP 30 m GSD, including the non-uniformity caused by spectrometer co-registration, keystone and telescope effects. The conversion to TOA radiance and DNs is performed by the atmospheric, spectral and radiometric modules afterwards. The branch *1b* of the simulation was applied to the Barrax agricultural site in Central Spain (39.0°N, -2.1°E) and to the Demmin area, in Northern Germany (53.9°N, 13.1°E), represented in Figs. 5(b) and 5(c), respectively. PROBA/CHRIS data with GSD=34 m were used as input in this case, so only an area of approximately 15 km×15 km was simulated. No simulation of the instrument MTF and spatial aberrations have been performed on them. The same is true for the Munich alpine foreland multitemporal series in Figs. 5(d)-5(f). Landsat data from three different acquisition dates were used as input. Different cloud covers were simulated for the three dates. Temporal changes in surface conditions can be seen.
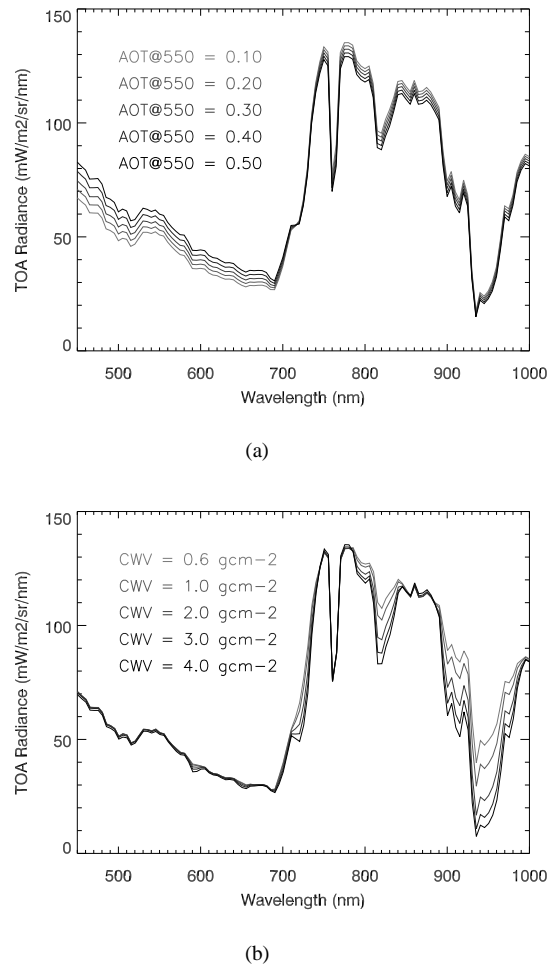

(a)

(b)

Fig. 6. Simulated EnMAP-like VNIR TOA radiance spectra for different (a) aerosol optical thickness and (b) columnar water vapor content.

The simulation of different atmospheric conditions, especially in terms of aerosol and water vapor loadings, is very useful in the development and validation of atmospheric correction algorithms. An example of simulated EnMAP-like VNIR TOA radiance spectra for a green vegetation target and different aerosol and water vapor contents is depicted in Fig. 6. The spectra are taken from the same pixel of the simulated Barrax data set. Radiometric noise is included in the simulations. The impact of aerosol scattering at the shortest wavelengths can be observed in Fig. 6(a), while the variation of the depth of the 940 nm absorption feature is observed in Fig. 6(b).

The simulation of instrumental noise and data non-uniformity in the spatial and spectral domains is necessary for the optimization of the instrument specifications. Simulated spatially coherent and non-coherent instrumental noise is illustrated in Fig. 7. The ratio of two correlated bands in the blue from the Barrax site is calculated in order to enhance the impact of noise. The ratio generated from noise-free data is displayed on the right hand side, while the one from noisy data is on the left hand side. Both the vertical striping and the non-coherent noise can be noticed despite the relatively high

(a) Makhtesh Ramon, RGB={2200,800,450}nm

(b) Barrax, RGB={660,550,450}nm

(c) Demmin, RGB={2200,800,450}nm

(d) Munich (6-Jul-06), RGB={660,550,450}nm

(e) Munich (22-Jul-06), RGB={660,550,450}nm
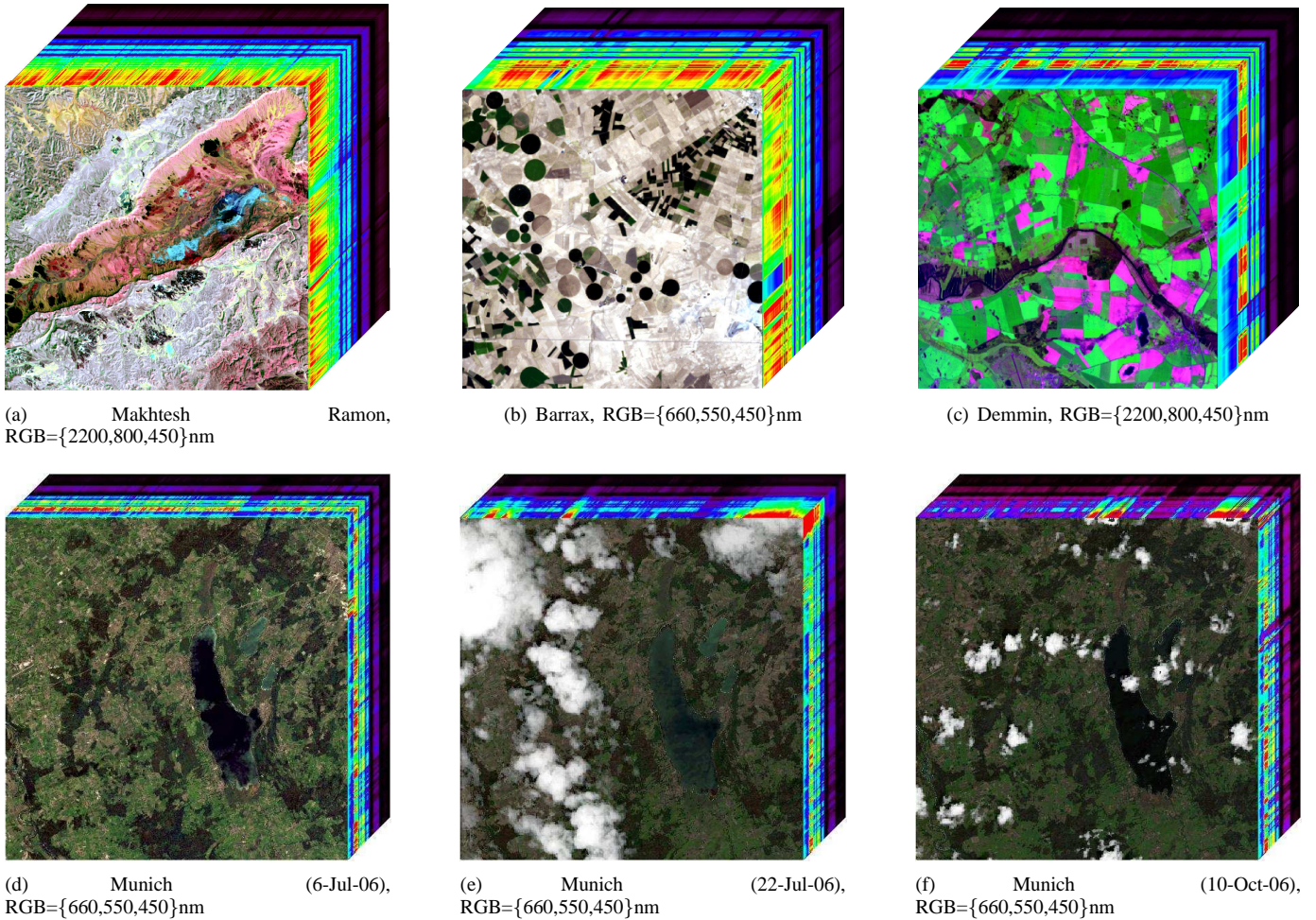
(f) Munich (10-Oct-06), RGB={660,550,450}nm

Fig. 5. Hypercubes generated from simulated EnMAP data at four different sites: the Makhtesh Ramon geological site in Israel (30.57°N, 34.83°E), the Barrax agricultural site in Central Spain (39.0°N, -2.1°E), the Demmin area, in Northern Germany (53.9°N, 13.1°E), and the Munich alpine foreland in Southern Germany (48.1°N, 11.1°E). Three acquisition dates with different surface conditions and cloud covers were simulated in the Munich case.
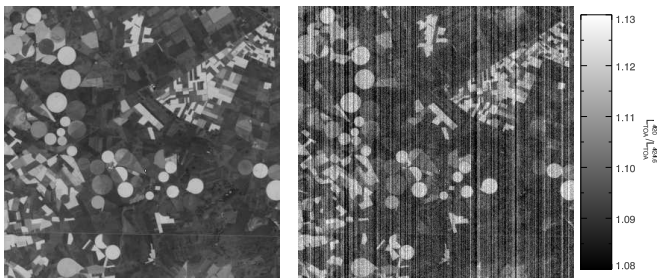
Fig. 7. Ratio between the first and second EnMAP spectral channels (at 420 and 424.6 nm, respectively) for noise-free (left) and noisy (right) simulated data at the Barrax site.

SNR of EnMAP of about 500:1 at the visible wavelengths.

EnMAP images with different noise levels were generated in order to assess the impact of instrumental noise in the information contained by hyperspectral data. The minimum noise fraction (MNF) transformation [44] was used to assess the information content as a function of noise. The MNF works decorrelating and normalizing the simulated data by means of a noise covariance matrix previously calculated. The resulting principal component images of the final principal component analysis from the MNF transformation with eigenvalues close to unity are considered to be dominated by noise. The images with eigenvalues greater than unity by a given threshold can be assumed to contain information about the target structure. The spectral SNR curve generated from the EnMAP specifications was scaled ×2 and ×3 to decrease the noise level. The results from the MNF transformation applied to the EnMAP VNIR spectrometer and the three simulated noise levels are shown in Fig. 8. The increase in data information content with higher SNR can be observed. This kind of simulation enables the assessment of the trade-off between spatial resolution and noise for the maximum information retrieval in a given application if the SNR is increased by the data spatial degradation [45].

Errors associated to data non-uniformity in the spatial dimension can be studied by means of the *1a* simulation branch in Fig. 1. Simultaneously to the spatial resampling of the input data by the convolution with the instrument MTF, optical aberrations such as keystone, spectrometer co-registration and telescope distortion are simulated. Simulated EnMAP data from the Makhtesh Ramon site were used for this purpose. The relative difference in the TOA radiance
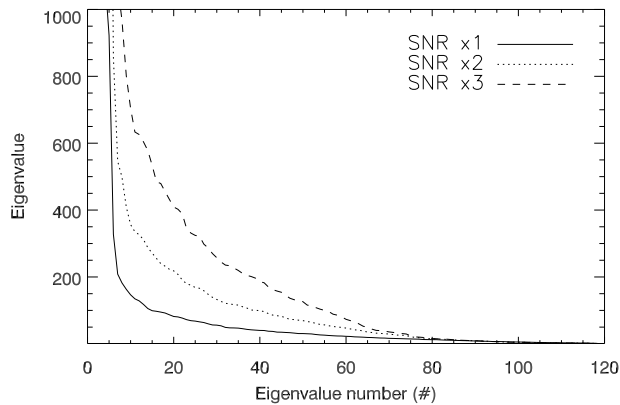
Fig. 8. Plots of eigenvalues as a function of eigennumbers calculated from simulated data in the first EnMAP spectrometer at the Makhtesh Ramon site and three different noise levels.
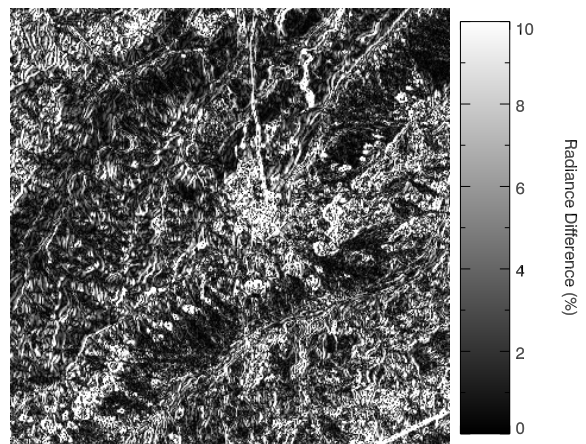

(a)

(b)

Fig. 9. Errors associated to the spatial non-uniformity of the data. A subset from the Makhtesh Ramon simulated image is displayed in (a), while the difference between the two spectrometers in the spectral overlap region (900 nm) is shown in (b).

image from two spectral channels centered at the 900 nm wavelength in the spectral overlap region, one from each of the EnMAP spectrometers, is displayed in Fig. 9. Only a subset of 400×400 pixels of the complete area in Fig. 5(a) is displayed. Deviations in pixel coordinates resulting from the three simulated spatial non-uniformity effects range from 0.9 to 1.4 pixels. The largest proportion of the difference comes from the errors in the spectrometer co-registration (which was almost 1.2 pixels) associated to the EnMAP two-slit design. As expected, errors increase with the heterogeneity of the area. Spatial patterns with abrupt borders at the reference image in Fig. 9(a) can be recognized in the calculated difference image in Fig. 9(b). Differences in radiance up to 10-15% between the two spectrometers can be stated. Spatially homogeneous areas will give much smaller errors. This is analogous to the fact that errors in radiance due to spectral non-homogeneity is relatively more important inside than outside atmospheric absorption features.

It has been estimated that the error caused by keystone and smile effects at the edges of the image across-track direction can be comparable to that due to co-registration. This is illustrated in Fig. 10. Makhtesh Ramon data with either keystone or smile and spectral shift as only non-uniformity source were simulated and compared to "ideal" uniform data. The curves in Fig. 2 and Fig. 4 were used for the simulation of keystone and smile, respectively. The results are plotted for two reference wavelengths, 450 and 900 nm, in the EnMAP VNIR spectrometer. The data were averaged in the along-track direction to minimize the effect of instrumental noise and surface background. Radiance errors due to keystone of up to 8% at the edges of the across-track dimension were derived at 450 nm, while those errors become smaller at 900 nm. This difference is explained by the larger keystone at the shortest wavelengths, as depicted in Fig. 2. The calculated error disappears at certain across-track positions, in which the input keystone curves cross the zero value.

Errors of a similar magnitude at the edges of the across-track direction are found in the case of smile and spectral
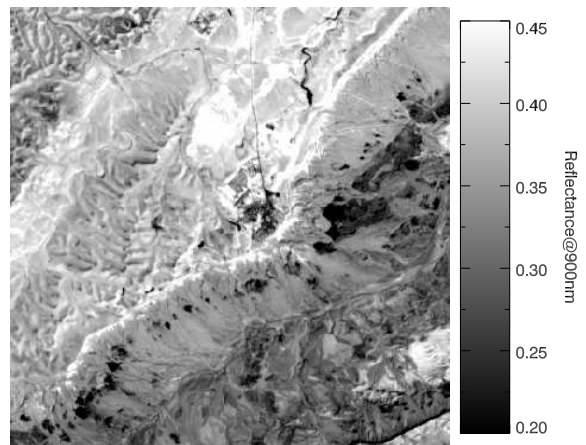
shift for the 900 nm band, while those errors are smaller at 450 nm. This is explained by the higher impact of spectral non-uniformity on spectral regions with abrupt spectral variations, as those due to atmospheric absorptions. The 900 nm channel is strongly affected by the water vapor absorption feature centered at 940 nm, while only residual atmospheric absorptions affect the blue channel at 450 nm. The bias of about 2% in the calculated error at 900 nm is due to the simulated overall spectral shift of 1 nm in the input smile curves.

IV. SUMMARY

A new tool for the simulation of optical remote sensing data has been presented in this paper. It has been developed during the definition phase of the EnMAP German hyperspectral mission in order to assist the system concept definition. It will also be used in the future for the generation of an EnMAP-like data base to serve as a basis for pre-processing and scientific algorithms development.

The scene simulator is built according to a modular structure. Five main processing modules are used for the derivation of the final TOA radiance and DN images. The first one is the
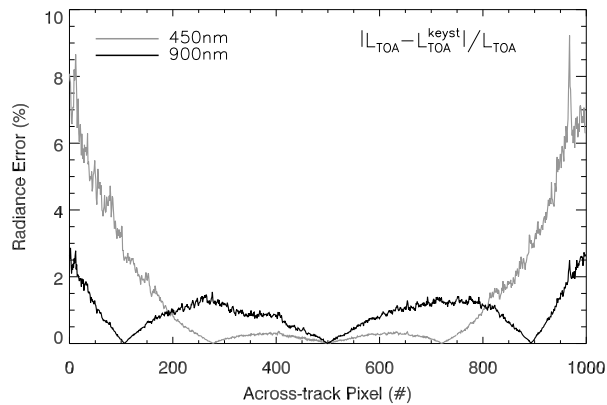
(a) Keystone
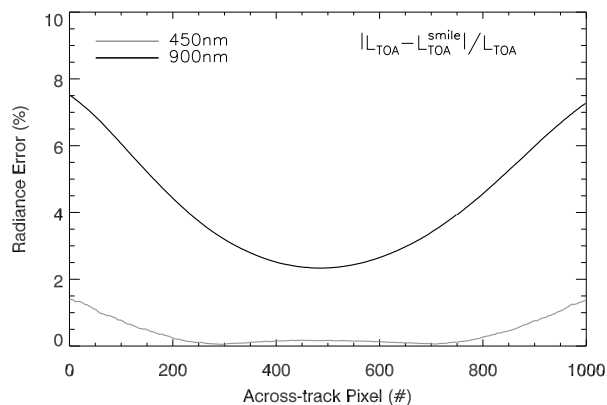
(b) Smile + Spectral shift

Fig. 10. Simulated data non-uniformity on the Makhtesh Ramon site in the spatial and spectral domain. Radiance errors are calculated after averaging in the along-track direction. Errors due to the keystone curves in Fig. 2 are plotted in (a), while errors due to the smile and spectral shift simulated with the curves in Fig. 4 are displayed in (b).

so-called reflectance module. It receives as input reflectance images from existing sensors and spectral libraries, and derives reflectance maps at high spectral resolution (1 nm for EnMAP). Depending on the input data, those reflectance maps are generated at the EnMAP 30 m GSD (e.g. PROBA/CHRIS and Landsat) or at 3-5 m resolution (e.g. SPOT and airborne data). In the second case, the resulting oversampled reflectance data are used to simulate the spatial convolution by the instrument MTF and data non-uniformity in the spatial domain through spectrometer co-registration, keystone and telescope distortion effects by the spatial module. Atmospheric radiative transfer effects are simulated by the atmospheric module for a user-defined scenario, given by illumination and observation geometry, atmospheric conditions and horizontal variations of AOT, CWV, surface elevation and cloud covers and shadows, in order to generate high spectral resolution data at 30 m GSD. The spectral module performs then the spectral convolution to the instrument spectral configuration. In the case of EnMAP this means two separate spectrometers with a spectral overlap window at 900-1000 nm, the spectral response function given

by Gaussian functions with SSI and FWHM varying non-linearly along the covered spectral range between 4 and 12 nm. Smile and spectral shift effects are simulated at the spectral convolution step. The final step in the simulation process is the simulation of instrumental noise and the conversion to DN data. Coherent and non-coherent noise is simulated according to a given SNR curve provided by the instrument specifications or a proposed instrument design. The conversion to DN data is performed by the application of calibration coefficients, gain and offset. Those are generated by assuming a given radiometric resolution and an instrument linear response between given maximum and minimum radiance levels.

The utility of the simulator has been shown in the second part of the paper. Several examples from simulated data and possible study cases have been displayed. The impact of varying aerosol and columnar water vapor on the VNIR region, the interrelation between SNR and information content, and an estimation of errors in radiance associated to data non-uniformity in the spatial domain, keystone and smile effects have been described. In particular, deviations of up to 10-15% between the VNIR and SWIR spectrometers have been calculated for the Makhtesh Ramon site and given co-registration, keystone and telescope distortion figures. Comparable errors are found at the edges of the image across-track direction for keystone and smile effects at that site and two wavelengths.

REFERENCES

[1] A. F. H. Goetz, G. Vane, J. E. Salomon, and B. N. Rock, "Imaging spectroscopy for Earth remote sensing," *Science*, vol. 228, pp. 1147–1153, 1985.
[2] G. Vane and A. F. H. Goetz, "Terrestrial imaging spectroscopy for Earth remote sensing," *Remote Sensing of Environment*, vol. 24, pp. 1–29, 1988.
[3] M. Schaepman et al., "The future of imaging spectroscopy – prospective technologies and applications," in *Proceedings of the International Geoscience and Remote Sensing Symposium (IGARSS)*, Denver, CO, USA, July 2006.
[4] R. O. Green, M. Eastwood, C. Sarture, T. Chrien, M. Aronsson, B. Chippendale, J. Faust, B. Pavri, C. Chovit, M. Solis, M. Olah, and O. Williams, "Imaging spectroscopy and the airborne visible/infrared imaging spectrometer (AVIRIS)," *Remote Sensing of Environment*, vol. 65, pp. 227–248, 1998.
[5] G. Vane, R. O. Green, T. G. Chrien, H. T. Enmark, E. G. Hansen, and W. M. Porter, "The Airborne Visible/Infrared Imaging Spectrometer (AVIRIS)," *Remote Sensing of Environment*, vol. 44, pp. 127–143, 1993.

[6] T. Cocks, R. Jenssen, A. Stewart, I. Wilson, and T. Shields, "The hymap airborne hyperspectral sensor: the system, calibration and performance," in *Proceedings of the First EARSeL Workshop on Imaging Spectroscopy*, Remote Sensing Laboratories, University of Zurich, Ed., Zurich, Switzerland, 1998, pp. 37–42.

[7] A. Mueller, R. Richter, M. Habermeyer, S. Dech, K. Segl, and H. Kaufmann, "Spectroradiometric requirements for the reflective module of the airborne spectrometer ARES," *IEEE Geoscience and Remote Sensing Letters*, vol. 2, pp. 329–332, 2005.

[8] K. I. Itten, M. Schaepman, L. D. Vos, L. Hermans, D. Schläpfer, and F. Droz, "APEXAirborne PRISM Experiment: a new concept for an airborne imaging spectrometer," in *Proceedings of the Third International Airborne Remote Sensing Conference and Exhibition*, Copenhagen, Denmark, 1997, pp. 181–188.

[9] S. G. Ungar, J. S. Pearlman, J. A. Mendenhall, and D. Reuter, "Overview of the Earth Observing One (EO-1) mission," *IEEE Transactions on Geoscience and Remote Sensing*, vol. 41, pp. 1149–1159, 2003.

[10] M. J. Barnsley, J. J. Settle, M. Cutter, D. Lobb, and F. Teston, "The PROBA/CHRIS mission: a low-cost smallsat for hyperspectral, multi-angle, observations of the Earth surface and atmosphere," *IEEE Transactions on Geoscience and Remote Sensing*, vol. 42, pp. 1512–1520, 2004.

[11] H. Kaufmann, K. Segl, L. Guanter, S. Hofer, K.-P. Foerster, T. Stuffler, A. Mueller, R. Richter, H. Bach, P. Hostert, and C. Chlebek, "Environmental Mapping and Analysis Program (EnMAP) – Recent Advances and Status," in *Proceedings of the International Geoscience and Remote Sensing Symposium (IGARSS)*, Boston, MA, USA, July 2008.

[12] R. O. Green, "Spectral calibration requirement for Earth-looking imaging spectrometers in the solar-reflected spectrum," *Applied Optics*, vol. 37, pp. 683–690, 1998.

[13] ——, "Atmospheric water vapor sensitivity and compensation requirement for Earth-looking imaging spectrometers in the solar-reflected spectrum," *Journal of Geophysical Research*, vol. 106, pp. 17 443–17 452, 2001.

[14] A. F. H. Goetz, B. C. Kindel, M. Ferri, and Z. Qu, "HATCH: Results from simulated radiances, AVIRIS and Hyperion," *IEEE Transactions on Geoscience and Remote Sensing*, vol. 41, pp. 1215–1222, 2003.

[15] E. Ben-Dor, B. C. Kindel, and A. F. H. Goetz, "Quality assessment of several methods to recover surface reflectance using synthetic imaging spectroscopy data," *Remote Sensing of Environment*, vol. 90, pp. 389–404, 2004.

[16] J. Nieke, D. Schläpfer, F. Dell'Endice, J. Brazile, and K. I. Itten, "Uniformity of imaging spectrometry data products," *IEEE Transactions on Geoscience and Remote Sensing*, vol. 46, pp. 3326–3336, 2008.

[17] D. Schläpfer, J. Nieke, and K. I. Itten, "Spatial PSF non-uniformity effects in airborne pushbroom imaging spectrometry data," *IEEE Transactions on Geoscience and Remote Sensing*, vol. 45, pp. 458–468, 2007.

[18] J. P. Kerekes and D. A. Landgrebe, "Simulation of optical remote sensing systems," *IEEE Transactions on Geoscience and Remote Sensing*, vol. 27, pp. 762–771, 1989.

[19] J. P. Kerekes and J. E. Baum, "Spectral imaging system analytical model for subpixel object detection," *IEEE Transactions on Geoscience and Remote Sensing*, vol. 40, pp. 1088–1101, 2002.

[20] ——, "Full-spectrum spectral imaging system analytical model," *IEEE Transactions on Geoscience and Remote Sensing*, vol. 43, pp. 571–580, 2005.

[21] J. R. Schott, S. D. Brown, R. V. Raqueño, H. N. Gross, and G. Robinson, "An advanced synthetic image generation model and its application to multi/hyperspectral algorithm development," *Canadian Journal of Remote Sensing*, vol. 25, pp. 99–111, 1999.

[22] A. Börner, L. Wiest, P. Keller, R. Reulke, R. Richter, M. Schaepman, and D. Schläpfer, "SENSOR: a tool for the simulation of hyperspectral remote sensing systems," *ISPRS Journal of Photogrammetry and Remote Sensing*, vol. 55, pp. 299–312, 2001.

[23] W. Verhoef and H. Bach, "Simulation of hyperspectral and directional radiance images using coupled biophysical and atmospheric radiative transfer models," *Remote Sensing of Environment*, vol. 87, pp. 23–41, 2003.

[24] ——, "Coupled soil-leaf-canopy and atmosphere radiative transfer modeling to simulate hyperspectral multi-angular surface reflectance and TOA radiance data," *Remote Sensing of Environment*, vol. 109, pp. 166–182, 2007.

[25] R. L. Sundberg, S. Richtsmeier, and R. Haren, "Full optical spectrum hyperspectral scene simulation," in *Proceedings of the International Geoscience and Remote Sensing Symposium (IGARSS)*, Seoul, Korea, July 2005.

[26] B. Sang, J. Schubert, S. Kaiser, V. Mogulsky, C. Neumann, K.-P. Förster, S. Hofer, T. Stuffler, H. Kaufmann, A. Müller, T. Eversberg, and C. Chlebek, "The EnMAP hyperspectral imaging spectrometer: instrument concept, calibration, and technologies," in *Proceedings of SPIE Conf. Imaging Spectrometry XIII*, vol. 7086, 2008.

[27] M. Arnaud and M. M. Leroy, "SPOT 4: a new generation of SPOT satellites," *ISPRS Journal of Photogrammetry and Remote Sensing*, vol. 46, pp. 205–215, 1991.

[28] P. Mouroulis, R. O. Green, and T. G. Chrien, "Design of pushbroom imaging spectrometers for optimum recovery of spectroscopic and spatial information," *Applied Optics*, vol. 39, pp. 2210–2220, 2000.

[29] B. Markham, J. Storey, D. Williams, and J. Irons, "Landsat sensor performance: history and current status," *IEEE Transactions on Geoscience and Remote Sensing*, vol. 42, pp. 2691–2694, 2004.

[30] T. Feingersh, E. Ben-Dor, and J. Portugali, "Construction of synthetic spectral reflectance of remotely sensed imagery for planning purposes," *Environmental Modelling & Software*, vol. 22, pp. 335–348, 2007.

[31] C. L. Lawson and R. J. Hanson, *Solving Least Squares Problems*. Prentice Hall, 1974.

[32] F. E. Nicodemus, J. C. Richmond, J. J. Hsia, I. W. Ginsberg, and T. Limperis, "Geometrical considerations and nomenclature for reflectance." National Bureau of Standards, US Department of Commerce, Washington, DC, USA, Tech. Rep., 1977.

[33] D. Tanré, M. Herman, and P. Y. Deschamps, "Influence of the atmosphere on space measurements of directional properties," *Applied Optics*, vol. 21, pp. 733–741, 1983.

[34] A. Berk, G. P. Anderson, P. K. Acharya, M. L. Hoke, J. H. Chetwynd, L. S. Bernstein, E. P. Shettle, M. W. Matthew, and S. M. Adler-Golden, "MODTRAN4 Version 3 Revision 1 User's Manual," Air Force Research Laboratory, Hanscom Air Force Base, MA, USA, Tech. Rep., 2003.

[35] A. Berk, L. S. Bernstein, G. P. Anderson, P. K. Acharya, D. C. Robertson, J. H. Chetwynd, and S. M. Adler-Golden, "MODTRAN cloud and multiple scattering upgrades with application to AVIRIS," *Remote Sensing of Environment*, vol. 65, pp. 367–375, 1998.

[36] L. Guanter, R. Richter, and H. Kaufmann, "On the application of the MODTRAN4 atmospheric radiative transfer code to optical remote sensing," *International Journal of Remote Sensing*, 2008, in press.

[37] D. Tanré, M. Herman, and P. Y. Deschamps, "Influence of the background contribution upon space measurements of ground reflectances," *Applied Optics*, vol. 20, pp. 3676–3684, 1981.

[38] E. F. Vermote, D. Tanré, J. L. Deuzé, M. Herman, and J. J. Morcrette, "Second Simulation of the Satellite Signal in the Solar Spectrum, 6S: An overview," *IEEE Transactions on Geoscience and Remote Sensing*, vol. 35, pp. 675–686, 1997.

[39] A. Sei, "Analysis of adjacency effects for two Lambertian half-spaces," *International Journal of Remote Sensing*, vol. 28, pp. 1873–1890, 2007.

[40] P. N. Reinersman and K. L. Carder, "Monte Carlo simulation of the atmospheric point-spread function with an application to correction for the adjacency effect," *Applied Optics*, vol. 20, pp. 4453–4471, 1995.

[41] F. Fell and J. Fischer, "Numerical simulation of the light field in the atmosphere-ocean system using the matrix-operator method," *Journal of Quantitative Spectroscopy and Radiative Transfer*, vol. 69, pp. 351–388, 2001.

[42] L. Gómez-Chova, G. Camps-Valls, J. Amorós-López, L. Guanter, L. Alonso, J. Calpe-Maravilla, and J. Moreno, "New cloud detection algorithm for multispectral and hyperspectral images: Application to ENVISAT/MERIS and PROBA/CHRIS sensors," in *Proceedings of the International Geoscience and Remote Sensing Symposium (IGARSS)*, Denver, CO, USA, July 2006.

[43] L. Gómez-Chova, G. Camps-Valls, J. Calpe-Maravilla, L. Guanter, and J. Moreno, "Cloud-screening algorithm for ENVISAT/MERIS multispectral images," *IEEE Transactions on Geoscience and Remote Sensing*, vol. 45, pp. 4105–4118, 2007.

[44] A. A. Green, M. Berman, P. Switzer, and M. D. Craig, "A transformation for ordering multispectral data in terms of image quality with implications for noise removal," *IEEE Transactions on Geoscience and Remote Sensing*, vol. 26, pp. 65–74, 1988.

[45] R. Green and J. Boardman, "Exploration of the relationship between information content and signal-to-noise ratio and spatial resolution in AVIRIS spectral data," in *AVIRIS Airborne Geoscience Workshop Proceedings*, Jet Propulsion Laboratory, Ed., Pasadena, CA, USA, 2000.